[6] Kutler, P., Warming, R. F., and Lomax, H., "Computation of Space Shuttle Flowfields Using Noncentered Finite-Difference Schemes," *AIAA Journal*, Vol. 11, No. 2, Feb. 1973, pp. 196–204.
[7] Lomax, H., "An Operational Unification of Finite Difference Methods for the Numerical Integration of Ordinary Differential Equations," TR-262, 1967, NASA.
[8] Richtmyer, R. D., and Morton, K. W., *Difference Methods for Initial-Value Problems*, Wiley, New York, 1967.
[9] Burstein, S. Z., "Finite-Difference Calculations for Hydrodynamic Flows Containing Discontinuities," *Journal of Computational Physics*, Vol. 2, 1967, pp. 198–222.
[10] Ames, W. F., *Numerical Methods for Partial Differential Equations*, Barnes and Noble, New York, 1969.
[11] Ralston, A., "Runge-Kutta Methods with Minimum Error Bounds," *Mathematics of Computation*, Vol. 16, 1962, pp. 431–437.
[12] Hirt, C. W., "Heuristic Stability Theory for Finite-Difference Equations," *Journal of Computational Physics*, Vol. 2, 1968, pp. 339–355.
[13] Lomax, H., Kutler, P., and Fuller, F. B., "The Numerical Solution of Partial Differential Equations Governing Convection," AGARD-AG-146-70, 1970.
[14] Lax, P. D., "Weak Solutions of Nonlinear Hyperbolic Equations and Their Numerical Computation," *Communications on Pure and Applied Mathematics*, Vol. 7, 1954, pp. 159–193.
[15] Moretti, G., Grossman, B., and Marconi, F., Jr., "A Complete Numerical Technique for the Calculation of Three-Dimensional Inviscid Supersonic Flows," AIAA Paper, 72-192, San Diego, Calif., 1972.

FEBRUARY 1973 AIAA JOURNAL VOL. 11, NO. 2

Computation of Space Shuttle Flowfields Using Noncentered Finite-Difference Schemes

PAUL KUTLER,* R. F. WARMING,* AND HARVARD LOMAX†
NASA Ames Research Center, Moffett Field, Calif.

The three-dimensional supersonic flowfield surrounding a configuration representing a space shuttle orbiter is determined using a shock-capturing, finite-difference approach. The governing hyperbolic partial differential equations in cylindrical coordinates are normalized between the body and an outer boundary which completely encompasses the disturbed flow region. The equations are then cast in conservation-law form and integrated from an initial data plane downstream over the body using either a second- or third-order noncentered finite-difference scheme. Existing shocks that form as a result of protuberances such as the canopy or wing are captured automatically and do not require the use of any shock-fitting procedures. Numerical results are compared with experimental data to demonstrate the capability of the method to accurately predict the inviscid flowfield about shuttle-like configurations. Three-dimensional shock-shock intersections that result in a coalesced shock and a slip surface posed no problem for the numerical procedure.

Introduction

THE capability of computing numerically the inviscid flowfield structure surrounding a space shuttle vehicle (SSV) or some representative configuration at supersonic velocities is of considerable importance in the prediction of heat-transfer rates, boundary-layer effects, sonic booms, and the aerodynamic loads associated with such vehicles. The large angles of attack at which the SSV is designed to enter the earth's atmosphere, at least initially, result in large regions of embedded subsonic flow near the nose of the vehicle. In addition, the complicated geometry of the shuttle gives rise to a multishocked flowfield. The wing and canopy of a typical SSV configuration generate secondary and embedded shocks which, in some instances, intersect the main bow shock. Conventional sharp shock theories (those that isolate a shock and apply the Rankine-Hugoniot shock relations across it) are limited in their capability of handling the shock-shock intersection problem and the formation of all embedded shock waves. Consequently, our approach in tackling this complex problem is to use a shock-capturing technique which, unlike conventional sharp shock theories, is capable of numerically predicting the location and intensity of all predominant shock waves without the explicit use of any shock-fitting procedures. The success of the shock-capturing technique (SCT) in correctly predicting complicated, multishock flowfields has been demonstrated in Refs. 1 and 2.

For purposes of this analysis, a delta-wing shuttle configuration is modeled. It is known from wind-tunnel experiments that for moderate angles of attack of such a configuration the surrounding flowfield is entirely supersonic except for a small region near the nose. The governing three-dimensional steady flow equations are, therefore, hyperbolic and with suitable initial data this becomes a well-posed initial-value problem. The equations in conservation-law form are differenced using either a second- or third-order noncentered finite-difference scheme.[3] Then starting from an initial data plane near the nose of the body, the difference equations are integrated downstream over the body. The starting solutions are obtained by representing the nose of the vehicle by either a pointed cone or a blunt sphere-cone.

Noncentered algorithms[3] use, in general, forward or backward

Presented as Part III of AIAA Paper 72-193 at the AIAA 10th Aerospace Sciences Meeting, San Diego, Calif., January 17–19, 1972; submitted February 16, 1972; revision received September 21, 1972.
Index categories: Supersonic and Hypersonic Flow; Entry Vehicles and Landers.

* Research Scientist, Computational Fluid Dynamics Branch. Member AIAA.
† Chief, Computational Fluid Dynamics Branch. Member AIAA.

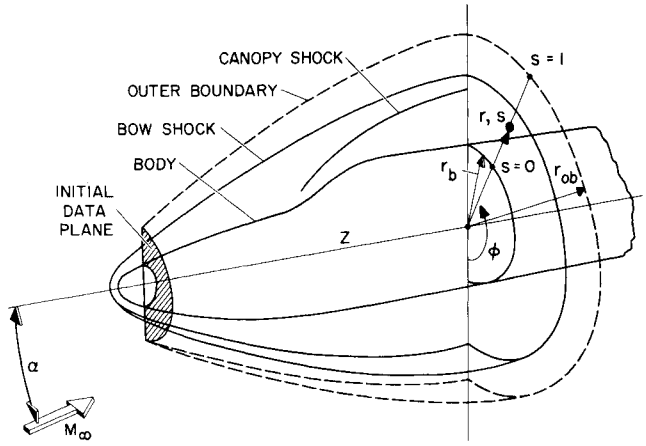

Fig. 1 Coordinate system for three-dimensional body.

difference quotients to approximate spatial derivatives. Noncentered schemes possess three advantages over conventional centered schemes: 1) the program logic is simpler, 2) the inclusion of a nonhomogeneous or source term into the finite-difference scheme is trivial, and 3) the scheme can be easily generalized to several space dimensions.

Numerical results have been carried out which compare solutions obtained using both the second- and third-order noncentered schemes. A critical comparison between the two, including shock definition, is made for a 15° half-angle cone at 5° angle of attack in Mach 5 flow. Detailed flowfield results are presented for a shuttlelike configuration with a pointed nose at zero incidence and a sphere-cone nose at 15.3° angle of attack both in Mach 7.4 flow. The numerical calculations are compared with experimental shadowgraphs obtained at the NASA Ames Research Center and show reasonably good agreement.

All computations were performed on an IBM 360-67 linked with a cathode-ray display tube (CRT). The CRT, with its man-machine interactive capability, was used to study the flowfield as it developed and to control any numerical instabilities that evolved.

Review of Governing Flow Equations

The gasdynamic equations for steady inviscid flow of a non-heat-conducting, perfect gas can be written in dimensionless, conservation-law form for cylindrical coordinates (z, r, ϕ) with velocity components (u, v, w) as follows

$$\partial\tilde{U}/\partial z+\partial\tilde{F}/\partial r+\partial\tilde{G}/\partial\phi+\tilde{H}=0 \tag{1}$$

where $\tilde{U}$, $\tilde{F}$, $\tilde{G}$, and $\tilde{H}$ are four-dimensional vectors defined by

$$\tilde{U}=\begin{vmatrix}\rho u\\ kp+\rho u^2\\ \rho uv\\ \rho uw\end{vmatrix},\quad \tilde{F}=\begin{vmatrix}\rho v\\ \rho uv\\ kp+\rho v^2\\ \rho vw\end{vmatrix},\quad \tilde{G}=\frac{1}{r}\begin{vmatrix}\rho w\\ \rho uw\\ \rho vw\\ kp+\rho w^2\end{vmatrix},$$

$$\tilde{H}=\frac{1}{r}\begin{vmatrix}\rho v\\ \rho uv\\ \rho(v^2-w^2)\\ 2\rho vw\end{vmatrix}$$

Equation (1) represents the continuity and three momentum equations in which pressure p and density ρ were made dimensionless with respect to freestream stagnation conditions, and velocity with respect to the maximum adiabatic velocity and where $k=(\gamma-1)/2\gamma$ and γ is the ratio of specific heats. Under the above conditions, the energy equation can be written in the dimensionless form

$$p=\rho(1-u^2-v^2-w^2) \tag{2}$$

The freestream conditions are simply a function of Mach number M_∞, angle of attack α, and γ, and are given by the following equations

$$p_\infty=\{1+[(\gamma-1)/2]M_\infty{}^2\}^{-\gamma/(\gamma-1)}$$
$$\rho_\infty=\{1+[(\gamma-1)/2]M_\infty{}^2\}^{-1/(\gamma-1)}$$
$$u_\infty=q_\infty\cos\alpha,\quad v_\infty=-q_\infty\sin\alpha\cos\phi,\quad w_\infty=q_\infty\sin\alpha\sin\phi$$

where

$$q_\infty=(u_\infty{}^2+v_\infty{}^2+w_\infty{}^2)^{1/2}=$$
$$\{[M_\infty{}^2(\gamma-1)/2]/[1+M_\infty{}^2(\gamma-1)/2]\}^{1/2}$$

In applying the SCT to three-dimensional problems it is desirable to analytically describe an outer boundary of the computational region. This outer boundary should completely envelop the disturbed region surrounding the body and preferably lie close to the outermost shock (see Fig. 1). This minimizes unnecessary differencing of points known to lie in the freestream. Shadowgraphs are useful in selecting the outer boundary, but not a necessity.

A nonorthogonal coordinate transformation is introduced which normalizes the distance between the body and outer boundary, i.e.,

$$z=z,\quad \phi=\phi,\quad s=(r-r_b)/(r_{ob}-r_b) \tag{3}$$

where r_b and r_{ob} are the cylindrical radii of the body and the outer boundary, respectively, and, in general

$$r_b=r_b(z,\phi)\quad\text{and}\quad r_{ob}=r_{ob}(z,\phi) \tag{4}$$

Applying the transformation (3) to Eq. (1) and rearranging in conservation-law form, there follows the final version of the equations to be differenced

$$\partial U/\partial z+\partial F/\partial s+\partial G/\partial\phi+H=0 \tag{5}$$

where

$$U=\tilde{U},\quad F=(\tilde{a}/\tilde{c})\tilde{U}+(1/\tilde{c})\tilde{F}+(\tilde{b}/\tilde{c})\tilde{G}$$
$$G=\tilde{G},\quad H=\tilde{H}-(\tilde{a}/\tilde{c})_s\tilde{U}-(1/\tilde{c})_s\tilde{F}-(\tilde{b}/\tilde{c})_s\tilde{G}$$

and

$$\frac{\tilde{a}}{\tilde{c}}=\frac{-r_{b_z}-s(r_{ob_z}-r_{b_z})}{r_{ob}-r_b},\quad \frac{1}{\tilde{c}}=\frac{1}{r_{ob}-r_b},\quad \frac{\tilde{b}}{\tilde{c}}=\frac{-r_{b_\phi}-s(r_{ob_\phi}-r_{b_\phi})}{r_{ob}-r_b}$$

$$(\tilde{a}/\tilde{c})_s=-\frac{r_{ob_z}-r_{b_z}}{r_{ob}-r_b},\quad (1/\tilde{c})_s=0,\quad (\tilde{b}/\tilde{c})_s=-\frac{r_{ob_\phi}-r_{b_\phi}}{r_{ob}-r_b} \tag{6}$$

The integration of Eq. (5) is performed with respect to z, since the equation is hyperbolic with respect to that coordinate. The flow variables p, ρ, u, v, and w are, therefore, determined from the components u_i of the conservative variable U. As was pointed out in Ref. 2, this necessitates the solution of five simultaneous algebraic equations.

Body and Outer Boundary Geometry

To facilitate the numerical computations, an approximation of the actual wing-body configuration is made using analytic functions. The z axis of the coordinate system shown in Fig. 1 is chosen to lie in the plane of symmetry and along the projection in that plane of the trace of the wing leading edge as illustrated in Fig. 2. The origin of the coordinate system $(z=0)$ is located at the nose of the vehicle. A typical cross section is approximated by two ellipses as shown in Fig. 2.

Thus, we write

$$r_b(z,\phi)=\frac{a(z)b(z)}{[b^2(z)\sin^2\phi+a^2(z)\cos^2\phi]^{1/2}} \tag{7}$$

where $a(z)$ and $b(z)$ represent the semimajor and semiminor axes of either the top or bottom ellipse. In this case $a_t(z)=a_b(z)$ and represents the wing-body variation with z as viewed in planform, while $b_t(z)$ and $b_b(z)$ describe the top and bottom body variations as seen from the side. The z axis is divided into intervals (z_{k-1}, z_k), not necessarily of equal length, and the functions $a(z)$ and $b(z)$ are approximated in each interval by a cubic polynomial; e.g.

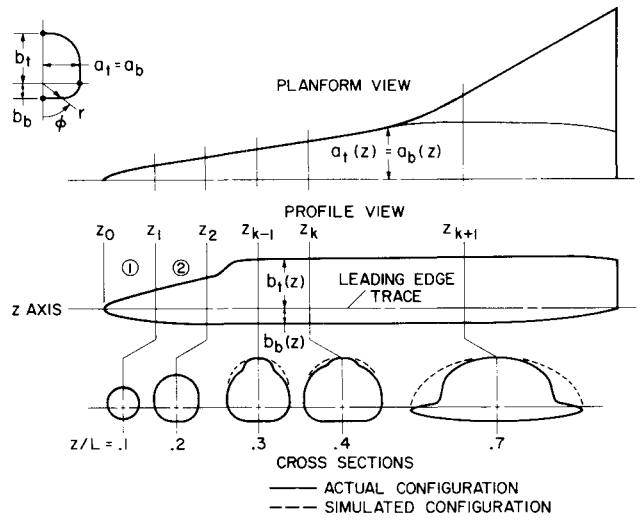

Fig. 2 Comparison of analytically described configuration with actual body shape.

$$a(z) = \sum_{p=0}^{3} \lambda_p (z - z_{k-1})^p; \quad (z_{k-1} \leqq z \leqq z_k) \tag{8}$$

The four coefficients λ_p are determined for each interval by matching $a(z)$ and its derivative da/dz with $r_b(z, \phi = 90°)$ and $\partial r_b(z, \phi = 90°)/\partial z$ at z_{k-1} and z_k. A similar procedure is used for the semiminor axis $b(z)$ for both the top and bottom ellipses. The partial derivatives $\partial r_b/\partial z$ and $\partial r_b/\partial \phi$ are thus continuous. However, the second derivatives are discontinuous. It is, therefore, only necessary to know the cylindrical radius of the body r_b and the slope $\partial r_b/\partial z$ at points z_k and z_{k-1} for the bottom, planform, and top surfaces in order to describe the body in this fashion. These data can be obtained from working drawings of a given configuration.

A comparison between an actual and simulated configuration used for this paper is shown in Fig. 2 for the planform and profile views and for various cross sections. In regions where the wing is predominant, the approximation of the upper surface is somewhat crude. However, for particular flight conditions, in which the angle of attack is large, the flow conditions on the lower surface can still be accurately predicted. The outer boundary that completely encompasses the disturbed region surrounding the vehicle is analytically described in a way analogous to that of the body, i.e., with longitudinal cubic polynomials and bielliptical cross sections.

Discretization and Initialization of Flow Region

The existence of a plane of symmetry ($\phi = 0°$, $180°$) reduces the computations by $\frac{1}{2}$, and consequently the disturbed region between the body and outer boundary need only be discretized in the half-plane as shown in Fig. 3a. Because the third-order difference scheme requires evaluation of the dependent variables at two points on either side of the point being computed, a boundary fringe, two mesh intervals wide, is established near the planes of symmetry, within the body, and in the freestream. This facilitates the orderly application of the differencing scheme, and eliminates special treatment at some of these points. The reflection principle is applied at the $\phi = 0°$ and $180°$ planes of symmetry. The points in the s direction are distributed equally $[\Delta s = 1/(NS-1) = \text{const}]$ between the body and outer boundary as are the points in the ϕ direction $[\Delta\phi = \pi/(N\phi - 3) = \text{const}]$ as shown in the computational plane of Fig. 3b.

The starting solution or initial data plane is obtained in either of two ways. The coded program is inherently capable of generating a pointed cone at angle-of-attack solution using the SCT. To start that solution all the grid points are initialized using values of the freestream variables. Once a converged solution is obtained, a control variable is switched and the integration is continued over the rest of the body. The second method of obtaining an initial data plane is to couple the program with an existing blunt-body code. In this case the inverse blunt-body code of Lomax and Inouye[4] is coupled with the method of characteristics scheme of Rakich[5] to yield the starting solution. A sphere-cone combination is used for the nose of the vehicle and this is smoothly transitioned with the bi-elliptical afterbody.

Finite-Difference Techniques

The ability of an SCT to accurately predict the location and intensity of all shock waves in addition to the continuous portion of the flowfield depends in part on the finite-difference scheme used. In Ref. 3, both second- and third-order non-centered finite-difference methods for solving hyperbolic partial differential equations were discussed.

The application of these schemes to three-dimensional supersonic flow problems is a severe test of their shock-capturing capability. For completeness and ease of coding we write out the schemes in detail below as applied to Eq. (5).

MacCormack's second-order scheme[3,6] is

$$U_{i,j}^{(1)} = U_{i,j}^n - \alpha_1 \left\{ \frac{\Delta z}{\Delta s}\left[(1-\varepsilon_s)F_{i+1,j}^n - (1-2\varepsilon_s)F_{i,j}^n - \varepsilon_s F_{i-1,j}^n\right] + \frac{\Delta z}{\Delta\phi}\left[(1-\varepsilon_\phi)G_{i,j+1}^n - (1-2\varepsilon_\phi)G_{i,j}^n - \varepsilon_\phi G_{i,j-1}^n\right] + \Delta z H_{i,j}^n \right\} \tag{9a}$$

$$U_{i,j}^{n+1} = \tfrac{1}{2}(U_{i,j}^n + U_{i,j}^{(1)}) - w_1 \left\{ \frac{\Delta z}{\Delta s}\left[\varepsilon_s F_{i+1,j}^{(1)} + (1-2\varepsilon_s)F_{i,j}^{(1)} + (\varepsilon_s - 1)F_{i-1,j}^{(1)}\right] + \frac{\Delta z}{\Delta\phi}\left[\varepsilon_\phi G_{i,j+1}^{(1)} + (1-2\varepsilon_\phi)G_{i,j}^{(1)} + (\varepsilon_\phi - 1)G_{i,j-1}^{(1)}\right] + \Delta z H_{i,j}^{(1)} \right\} \tag{9b}$$

where $\alpha_1 = 1$, $w_1 = \frac{1}{2}$, and

$$U_{i,j}^n = U(n\Delta z, i\Delta s, j\Delta\phi)$$
$$F_{i,j}^n = F(U_{i,j}^n, n\Delta z, i\Delta s, j\Delta\phi)$$
$$F_{i,j}^{(1)} = F^{(1)}(U_{i,j}^{(1)}, \ (n+\alpha_1)\Delta z, i\Delta s, j\Delta\phi) \quad \text{etc.}$$

This scheme allows four possible variations for replacing the space derivatives in the predictor and corrector steps

$$\begin{aligned} &\text{I:} \quad \varepsilon_s = 0, \quad \varepsilon_\phi = 0 \\ &\text{II:} \quad \varepsilon_s = 1, \quad \varepsilon_\phi = 1 \\ &\text{III:} \quad \varepsilon_s = 0, \quad \varepsilon_\phi = 1 \\ &\text{IV:} \quad \varepsilon_s = 1, \quad \varepsilon_\phi = 0 \end{aligned} \tag{10}$$

MacCormack[6] suggests that in applying this scheme for general flow problems, the four variations (I–IV) be cyclically

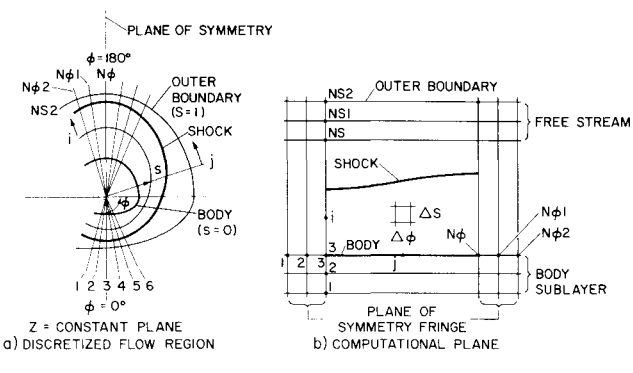

Fig. 3 Mesh description: a) discretized flow region, b) computational plane.

permuted to obtain unbiased results. It has been found, however, both in the current study and in the study of Ref. 1 that for shocks that move upward or away from the body in the computational plane, method I tends to yield better results near the shock by minimizing the post and precursor oscillations. It has also been found that method II is best for shocks that move toward the body in the computational plane, and a permutation of methods I and II is best for shocks that remain stationary. The relative motion of the shock wave in the computational plane can be observed on the cathode ray tube and the appropriate method applied. It is, however, not mandatory that this approach be used, and quite successful results have been obtained by the sole use of method I. Since both the canopy and wing shocks tend to move upward in the computational plane, method I was used for the majority of the calculations.

The third-order finite-difference scheme developed in Ref. 3 is a three-step method that uses the first two steps of MacCormack's method. The algorithm can be written as

$$U^{(1)}_{i,j} = \text{same as right side of (9a) with } \alpha_1 = \tfrac{2}{3} \tag{11a}$$

$$U^{(2)}_{i,j} = \text{same as right side of (9b) with } \alpha_1 = \tfrac{2}{3} \text{ and } w_1 = \tfrac{1}{3} \tag{11b}$$

$$\begin{aligned} U^{n+1}_{i,j} = {} & U^n_{i,j} - [(\omega_s)^n_{i+1/2,j}/24] \times \\ & [U^n_{i+2,j} - 3U^n_{i+1,j} + 3U^n_{i,j} - U^n_{i-1,j}] + \\ & [(\omega_s)^n_{i-1/2,j}/24][U^n_{i+1,j} - 3U^n_{i,j} + 3U^n_{i-1,j} - U^n_{i-2,j}] - \\ & [(\omega_\phi)^n_{i,j+1/2}/24][U^n_{i,j+2} - 3U^n_{i,j+1} + 3U^n_{i,j} - U^n_{i,j-1}] + \\ & [(\omega_\phi)^n_{i,j-1/2}/24][U^n_{i,j+1} - 3U^n_{i,j} + 3U^n_{i,j-1} - U^n_{i,j-2}] - \\ & \tfrac{1}{24}[(\Delta z/\Delta s)(-2F^n_{i+2,j} + 7F^n_{i+1,j} - 7F^n_{i-1,j} + 2F^n_{i-2,j}) + \\ & (\Delta z/\Delta\phi)(-2G^n_{i,j+2} + 7G^n_{i,j+1} - 7G^n_{i,j-1} + 2G^n_{i,j-2}) + \\ & 6\Delta z H^n_{i,j}] - \tfrac{3}{8}(\Delta z/\Delta s)(F^{(2)}_{i+1,j} - F^{(2)}_{i-1,j}) + \\ & (\Delta z/\Delta\phi)(G^{(2)}_{i,j+1} - G^{(2)}_{i,j-1}) + 2\Delta z H^{(2)}_{i,j}] \end{aligned} \tag{11c}$$

It should be emphasized here that $U^{(1)}$, $U^{(2)}$, $F^{(1)}$, $F^{(2)}$, etc., are evaluated at the z coordinate $(n+\frac{2}{3})\Delta z$. The free parameter terms of Eq. (11c), i.e., the brackets with multiplicative coefficients ω_s and ω_ϕ, have been differenced conservatively in both the s and ϕ directions, and formulas for ω_s and ω_ϕ are given in a later section on stability. Since these terms represent a fourth-order difference operator (see Ref. 3), they do not affect the third-order accuracy of the algorithm. Any of the four possible variations of MacCormack's method are applicable for the first two steps (11a, b), and each is consistent with the third-order accuracy of the final step (11c).

Boundary Conditions

An important aspect in the successful application of a finite-difference technique is the proper treatment of the surface boundary conditions. There are numerous schemes available for satisfying the simple tangency condition at solid surfaces (see, e.g., Refs. 7–10). In this section a scheme is presented which was devised by Abbett,[11] and combines simplicity with accuracy. It treats the computation at the body in the same predictor-corrector fashion as the interior points and is, therefore, compatible with the rest of the calculations.

In applying Abbett's scheme one first predicts values of the flow variables (p, ρ, u, v, w) at $z^{n+1} = z^n + \Delta z$ using an Euler predictor and then corrects these quantities using simple compression or expansion waves to invoke the surface tangency condition exactly. The details for the present problem follow.

In predicting the flow variables at $z^{n+1} = z^n + \Delta z$, the following predictor scheme is used to difference Eq. (5) at the body ($i = 3$):

$$U^{(1)}_{3,j} = U^n_{3,j} - \frac{\Delta z}{\Delta s}(F^n_{4,j} - F^n_{3,j}) - \frac{\Delta z}{\Delta\phi} \times \left[\frac{\varepsilon_b}{2} G^n_{3,j+1} + (1-\varepsilon_b) G^n_{3,j} + \left(\frac{\varepsilon_b}{2} - 1\right) G^n_{3,j-1}\right] - \Delta z H^n_{3,j} \tag{12}$$

The s derivative is replaced by a first-order forward (away from body) finite-difference approximation while the ϕ derivative is replaced by either a second-order central difference ($\varepsilon_b = 1$) when the velocity component w is subsonic ($w < c$) or a first-order backward difference ($\varepsilon_b = 0$) when $w > c$ and in the positive ϕ direction. This physical differencing of the ϕ derivative makes the scheme consistent with the law of forbidden signals. Decoding the conservative variables, $U^{(1)}_{3,j}$, from Eq. (12) yields $p^{(1)}_{3,j}$, $\rho^{(1)}_{3,j}$, $u^{(1)}_{3,j}$, $v^{(1)}_{3,j}$, and $w^{(1)}_{3,j}$ at z^{n+1}.

Equation (4), which describes the body, can be rewritten as

$$f = r_b - r_b(z, \phi) = 0 \tag{13}$$

Thus the outward unit normal to the body is given by

$$\hat{n}_b = \frac{\nabla f}{|\nabla f|} = \frac{-r_{b_z}\hat{i}_z + \hat{i}_r - r_{b_\phi}\hat{i}_\phi/r_b}{(r_{b_z}{}^2 + 1 + r_{b_\phi}{}^2/r_b{}^2)^{1/2}} \tag{14}$$

where ∇ is the gradient operator. The surface tangency condition that must be satisfied everywhere on the body is

$$\vec{q} \cdot \hat{n}_b = 0 \tag{15}$$

or

$$-ur_{b_z} + v - wr_{b_\phi}/r_b = 0 \tag{16}$$

where the velocity vector in cylindrical coordinates is

$$\vec{q} = u\hat{i}_z + v\hat{i}_r + w\hat{i}_\phi \tag{17}$$

In general, the velocity vector

$$\vec{q}^{(1)}_{3,j} = u^{(1)}_{3,j}\hat{i}_z + v^{(1)}_{3,j}\hat{i}_r + w^{(1)}_{3,j}\hat{i}_\phi$$

predicted by Eq. (12) will not satisfy Eq. (16) and will be rotated out of the surface tangent plane by a small angle $\Delta\theta$. This angle can be determined from the following equation:

$$\Delta\theta = \sin^{-1}(\vec{q}^{(1)}_{3,j} \cdot \hat{n}_b / q^{(1)}_{3,j}) \tag{18}$$

where $q^{(1)}_{3,j}$ is defined to be the magnitude of $\vec{q}^{(1)}_{3,j}$. If $\Delta\theta$ is positive, this implies that an expansion is necessary to rotate $\vec{p}^{(1)}_{3,j}$ into the surface tangent plane, and if $\Delta\theta$ is negative a compression wave is required.

The following equation from NACA R-1135[12] (Eq. 174) expresses the ratio of final-to-initial static pressures for an expansion or compression through a small angle $\Delta\theta$

$$\begin{aligned} \frac{p^{n+1}_{3,j}}{p^{(1)}_{3,j}} = {} & 1 - \frac{\gamma(M^{(1)}_{3,j})^2}{[(M^{(1)}_{3,j})^2 - 1]^{1/2}}(\Delta\theta) + \gamma(M^{(1)}_{3,j})^2 \times \\ & \left\{\frac{(\gamma+1)(M^{(1)}_{3,j})^4 - 4[(M^{(1)}_{3,j})^2 - 1]}{4[(M^{(1)}_{3,j})^2 - 1]^2}(\Delta\theta)^2\right\} + 0[(\Delta\theta)^3] \end{aligned} \tag{19}$$

where

$$M^{(1)}_{3,j} = \frac{q^{(1)}_{3,j}}{c^{(1)}_{3,j}} \quad \text{and} \quad c^{(1)}_{3,j} = \left[\frac{\gamma-1}{2}\frac{p^{(1)}_{3,j}}{\rho^{(1)}_{3,j}}\right]^{1/2}$$

Substituting Eq. (18) into Eq. (19) yields the corrected value for the static pressure ($p^{n+1}_{3,j}$).

From the starting solution, all surface flow variables are known along with the value of entropy at the body, and since entropy is assumed to be constant over the entire body, that constant can be determined from

$$\left.\frac{p^n_{3,3}}{(\rho^n_{3,3})^\gamma}\right|_{\text{starting plane}} = \text{const} \quad \text{(nonconical flow)} \tag{20a}$$

When a cone solution is generated to be used as the starting solution, the surface entropy during the iteration procedure is calculated from

$$\frac{p^n_{4,3}}{(\rho^n_{4,3})^\gamma} = \text{const} \quad \text{(conical flow)} \tag{20b}$$

since the entropy throughout the shock layer in the windward plane ($j = 3$) is known to be constant. After the cone solution has converged and the afterbody is to be calculated, Eq. (20a) is employed to evaluate the constant.

Under the assumption of constant entropy along the body, the density $\rho^{n+1}_{3,j}$ can, therefore, be calculated from the equation

$$\rho^{n+1}_{3,j} = (p^{n+1}_{3,j}/\text{const})^{1/\gamma} \tag{21}$$

The velocity magnitude $q^{n+1}_{3,k}$ can then be determined from the energy equation (2) as

$$q_{3,j}^{n+1} = (1 - p_{3,j}^{n+1}/\rho_{3,j}^{n+1})^{1/2} \tag{22}$$

Finally, it is necessary to determine the individual components of $\vec{q}_{3,j}^{\,n+1}$. Since $\vec{q}_{3,j}^{(1)}$ was rotated through an angle $\Delta\theta$ in the plane of $\hat{n}_b$ and $\vec{q}_{3,j}^{(1)}$, it follows that the direction of the final velocity $\vec{q}_{3,j}^{\,n+1}$ must be in the direction of the vector $\vec{q}_{3,j}^{(1)} - (\vec{q}_{3,j}^{(1)} \cdot \hat{n}_b)\hat{n}_b$. Thus

$$\vec{q}_{3,j}^{\,n+1} = q_{3,j}^{n+1}\,\hat{n}_t \tag{23}$$

where

$$\hat{n}_t = \frac{\vec{q}_{3,j}^{(1)} - (q_{3,j}^{(1)} \cdot \hat{n}_b)\hat{n}_b}{|\vec{q}_{3,j}^{(1)} - (\vec{q}_{3,j}^{(1)} \cdot \hat{n}_b)\hat{n}_b|} \tag{24}$$

The velocity components obtained from Eq. (23) are

$$u_{3,j}^{n+1} = q_{3,j}^{n+1}(u_{3,j}^{(1)} + r_{b_z} M/N)/L \tag{25a}$$

$$v_{3,j}^{n+1} = q_{3,j}^{n+1}(v_{3,j}^{(1)} - M/N)/L \tag{25b}$$

$$w_{3,j}^{n+1} = q_{3,j}^{n+1}\left(w_{3,j}^{(1)} + \frac{r_{b_\phi}}{r_b} M/N\right)\Big/ L \tag{25c}$$

where

$$M = (-u_{3,j}^{(1)}\, r_{b_z} + v_{3,j}^{(1)} - w_{3,j}^{(1)}\, r_{b_\phi}/r_b)/N$$

$$N = (r_{b_z}{}^2 + 1 + r_{b_\phi}/r_b{}^2)^{1/2}$$

$$L = \left\{ (u_{3,j}^{(1)} + r_{b_z} M/N)^2 + (v_{3,j}^{(1)} - M/N)^2 + \left(w_{3,j}^{(1)} + \frac{r_{b_\phi}}{r_b}\frac{M}{N}\right)^2 \right\}^{1/2}$$

This boundary condition scheme encountered no difficulty with rapid changes in the body geometry such as found near the canopy and wing leading edge. The scheme passed with ease through the formation of both the canopy and wing leading edge shocks. For simple two-dimensional test cases, it has been compared with other techniques[11] currently in use, including reflection, extrapolation, method of characteristics, Kentzer's method,[9] and Thomas' method.[7]

Stability Analysis

It is necessary in numerical techniques to select a step size small enough to be commensurate with the stability bound, but yet large enough to finish the computation with a minimum of computer time. Use of the largest possible step size for hyperbolic equations insures that the finite-difference scheme is as nearly compatible with the method of characteristics or the perfect shift condition as possible.[3,13] To get a bound on the value the step size should have, many authors[14,15] rely on amplification matrix theory because of its ability to conservatively and quickly predict a stability condition. The method is based on a locally linear analysis of the governing partial differential equations coupled with a discrete harmonic analysis of the linear-difference scheme. The partial differential equation system, in this case Eq. (5), for the linear analysis is written in the form

$$\partial U/\partial z + P\,\partial U/\partial s + Q\,\partial U/\partial\phi + H = 0 \tag{26}$$

where P and Q are the Jacobian matrices ($\partial F/\partial U$ and $\partial G/\partial U$). The amplification matrix theory, at least for the two-dimensional z, s space, requires that

$$\Delta z/\Delta s \leq 1/(\sigma_p)_{\max} \qquad \sigma_p = |\sigma(P)|_{\substack{\text{local}\\ \max}} \tag{27}$$

where σ_p is defined to be the local maximum modulus of the eigenvalues of the matrix P for a given grid point in the field. It is the maximum of the local maximum eigenvalues in a particular $z = \text{const}$ plane that is needed in Eq. (27). A similar condition is obtained in z, ϕ space

$$\Delta z/\Delta\phi \leq 1/(\sigma_q)_{\max}, \quad \sigma_q = |\sigma(Q)|_{\substack{\text{local}\\ \max}} \tag{28}$$

This planar analysis has been shown[2] to give a good bound on the step size in multidimensional problems if Eqs. (27) and (28) are replaced by

$$\Delta z/\Delta s = \text{const}/(\sigma_p)_{\max} \tag{29a}$$

$$\Delta z/\Delta\phi = \text{const}/(\sigma_q)_{\max} \tag{29b}$$

where const < 1 can be varied during the computation and is usually assigned a value of approximately 0.9. When applying Eq. (29) to determine Δz, the mesh spacings Δs and $\Delta\phi$ are given. It is therefore necessary to determine the minimum Δz predicted by the two relations. This minimum Δz, which is recalculated after each integration step, is the one used for the succeeding step in the integration procedure.

The values σ_p and σ_q required in Eqs. (29) can be determined from the matrices P and Q. The five eigenvalues of P are

$$\sigma_{1,2}^P = \frac{1}{\tilde{c}}\left[\tilde{a} + \frac{u(v+\tilde{b}w/r) \pm c[(v+\tilde{b}w/r)^2 + (u^2-c^2)(1+\tilde{b}^2/r^2)]^{1/2}}{u^2-c^2}\right] \tag{30a}$$

$$\sigma_{3,4,5}^P = \frac{1}{\tilde{c}}[\tilde{a} + (v+\tilde{b}w/r)/u] \tag{30b}$$

and the five eigenvalues of Q are

$$\sigma_{1,2}^Q = \frac{1}{r}\left[\frac{uw \pm c(u^2+w^2-c^2)^{1/2}}{u^2-c^2}\right] \tag{31a}$$

$$\sigma_{3,4,5}^Q = w/(ur) \tag{31b}$$

Equations (30a) and (31a) can be recognized as the slopes of the characteristics in the z, s and z, ϕ planes, respectively, while Eqs. (30b) and (31b) represent the slopes of the streamlines in their respective planes. The maximum modulus of eigenvalues used in Eq. (29), therefore, are obtained from Eqs. (30a) and (31a), respectively,

$$\sigma_p = |\sigma(P)|_{\substack{\text{local}\\ \max}} = \max(|\sigma_1{}^P|, |\sigma_2{}^P|) \tag{32a}$$

$$\sigma_q = |\sigma(Q)|_{\substack{\text{local}\\ \max}} = \max(|\sigma_1{}^Q|, |\sigma_2{}^Q|) \tag{32b}$$

It remains to give explicit formulas for the free parameters ω_s and ω_ϕ appearing in the last step of the third-order scheme (11c). A constant free parameter $\omega = \omega_s = \omega_\phi$ can be used throughout the entire computation. However, our approach is to utilize a local variation of the free parameter in both the s and ϕ directions. The local value that each free parameter assumes is based on the local maximum eigenvalues σ_p and σ_q defined above. The stability analysis was based essentially on a one-dimensional analysis of the finite-difference equations and this seemed to be a plausible approach by virtue of the manner in which the second- and third-order noncentered algorithms are generalized from two to three space dimensions. Likewise, in lieu of a more complete theory, we determine the values of ω_s and ω_ϕ from the one-dimensional analysis of Ref. 3.

The values of ω_s and ω_ϕ required for Eq. (11) are determined as follows:

$$(\omega_s)_{i+1/2,j}^n = \omega_s[(v_s)_{i+1/2,j}^n] \tag{33}$$

where the brackets on the right side mean a function of the argument contained in the brackets and

$$v_s = (\Delta z/\Delta s)\sigma_p$$

Similarly, for ω_ϕ

$$(\omega_\phi)_{i,j+1/2}^n = \omega_\phi[(v_\phi)_{i,j+1/2}^n] \tag{34}$$

$$v_\phi = (\Delta z/\Delta\phi)\sigma_q$$

The requisite values of v_s and v_ϕ on the staggered mesh are found by the averages

$$(v_s)_{i+1/2,j}^n = \tfrac{1}{4}[(\sigma_p)_{i+2,j}^n + (\sigma_p)_{i+1,j}^n + (\sigma_p)_{i,j}^n + (\sigma_p)_{i-1,j}^n]\,\Delta z/\Delta s \tag{35a}$$

$$(v_\phi)_{i,j+1/2}^n = \tfrac{1}{4}[(\sigma_q)_{i,j+2}^n + (\sigma_q)_{i,j+1}^n + (\sigma_q)_{i,j}^n + (\sigma_q)_{i,j-1}^n]\,\Delta z/\Delta\phi \tag{35b}$$

For the functional forms (33) and (34), one can use formula (39) of Ref. 3 for minimum dissipation or formula (40) of Ref. 3 for minimum dispersion. The equation for minimum dispersion is recommended when crossing discontinuities. Thus for a given problem the free parameters can be defined on the basis of the local flow variables.

Table 1 Cone at angle-of-attack results ($M = 5, \sigma = 15°, \alpha = 5°$)

	p/p_∞			ρ/ρ_∞			v/u			w/u			$\tan\theta_s$		
	0	90	180	0	90	180	0	90	180	0	90	180	0	90	180
Babenko	5.401	3.618	2.433	3.001	2.254	1.698[a] 1.865[b]	0.2679	0.2679	0.2679	0	0.0823	0	0.3520	0.3676	0.3893
M.O.C.	5.397	3.615	2.436	2.999	2.253	1.699[a] 1.866[b]	0.2679	0.2679	0.2679	0	0.0820	0	0.3520	0.3674	0.3894
SCT1[c]	5.408	3.614	2.443	3.005	2.254	1.704[a]	0.2679	0.2679	0.2679	0	0.0831	0	0.3526	0.3678	0.3887
SCT1[d]	5.397	3.614	2.433	2.984	2.241	1.690[a]	0.2679	0.2679	0.2679	0	0.0870	0	0.3516	0.3685	0.3887

[a] Meridional value of density. The multivaluedness of certain flow variables is a result of the vortical singularity in the leeward plane of symmetry which is characteristic with conical flow problems.
[b] Normal value of density.
[c] Second order.
[d] Third order.

Numerical Results

To compare the relative accuracy of second- and third-order shock-capturing techniques and also to compare the results with existing sharp-shock methods, a simple cone flow problem was solved numerically. A 15° half-angle cone was oriented at 5° angle of attack in Mach 5 flow. Tabulated results of selected surface flow variables and shock locations are presented in Table 1 for both the second- and third-order schemes. The grid sizes for both second- and third-order calculations were equal and consisted of 29 points in the radial direction between the body and outer boundary and 19 points between the $\phi = 0°$ and 180° planes. Data obtained from Babenko[16] and the method of characteristics scheme (MOC) of Rakich[5] are also listed. A comparison of second- and third-order results based solely on the tabular values of Table 1 would not warrant the use of a third-order scheme.

Figure 4 shows a qualitative comparison between the second- and third-order cone results. Figures 4a–d were taken from the cathode-ray display tube (CRT) and each show radial pressure distribution plots at various meridional locations ($\phi = 0°$ implies the windward side). The results obtained using the second-order scheme are shown in Fig. 4a in which the characteristic post and precursor oscillations in the vicinity of the shock are evident. The shock wave for each meridian is spread over two mesh intervals and there is a well-defined shock layer.

Three sequences of results are presented which were obtained using the third-order method and various definitions of the free parameter. Figure 4b illustrates the flowfield obtained when the free parameters ω_s and ω_ϕ were held constant and equal to 2.4 and 0.3, respectively, throughout the entire disturbed region and for the complete iteration cycle. It is clearly evident that the fluctuations near the shock have been considerably reduced by the third-order scheme; however, the shock waves in each meridian are spread over a greater number of mesh intervals than those of the second-order results. The shock layer is now better defined than that of the second-order method because of the absence of the spurious fluctuations. To reduce the dissipative behavior of the third-order results of Fig. 4b, the variable free parameter concept was implemented. Thus, based on the local maximum eigenvalues of the gasdynamic equations in the radial and meridional directions, a local value of the free parameter for minimum dissipation or minimum dispersion was used to tune the solution. Figure 4c shows the results obtained when ω_s and ω_ϕ were defined for minimum dissipation. It is seen that when compared to Fig. 4b the weaker shock waves are sharper. In other calculations of the flowfields about more complicated configurations in which there was a large range in the magnitudes of the local eigenvalues, oscillations appeared in regions where the strongest part of the shock occurred when the free parameters were defined for minimum dissipation. In our subsequent computations, therefore, we used the minimum dispersion formula to define ω_s and ω_ϕ. The results obtained using the variable free parameters for minimum dispersion are shown in Fig. 4d. It is seen that there is a noticeable improvement over the constant free parameter results of Fig. 4b. A detailed plot of the pressure distribution in the leeward plane of symmetry ($\phi = 180°$) for each of the results discussed above is shown in Figs. 4e and f and are compared with that of Babenko.[16] The improvement in the shock-capturing ability of the third-order scheme over the second-order is apparent.

To test the SCT's ability to accurately predict the inviscid flowfield surrounding a typical space-shuttlelike orbiter and to

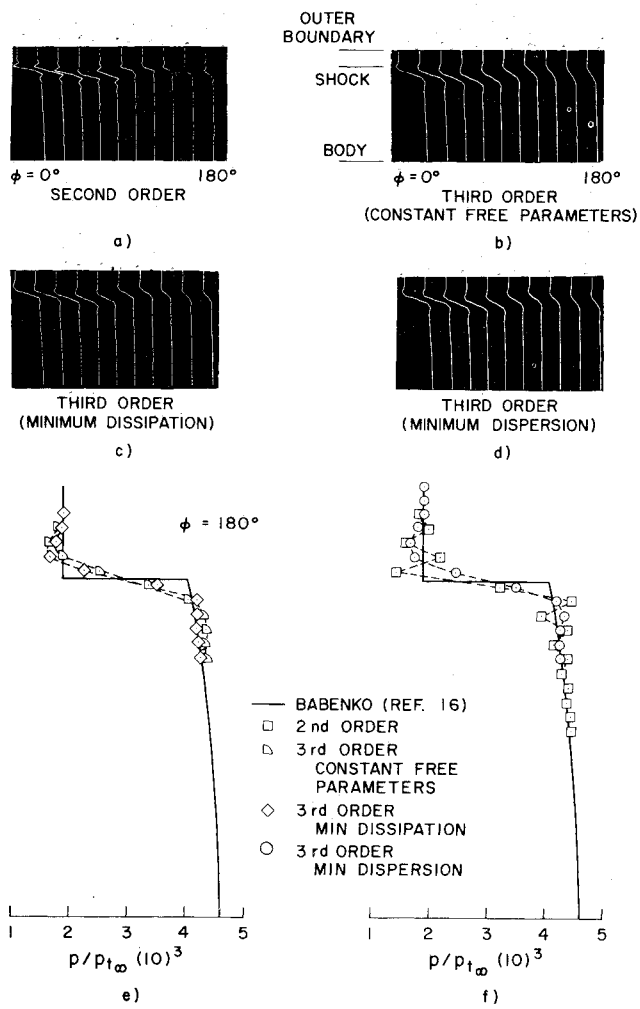

Fig. 4 Comparison of second- and third-order cone solutions; $M = 5$, $\alpha = 5°$, $\sigma = 15°$. a) second-order, b) third-order (constant free parameters), c) third-order (minimum dissipation), d) third-order (minimum dispersion), e) $\phi = 180°$, and f) $\phi = 180°$.

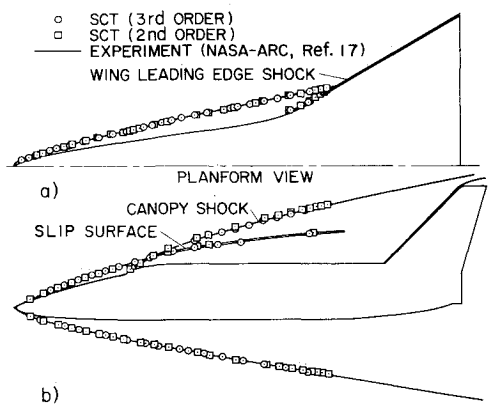

Fig. 5 Shock locations for shuttlelike configuration as predicted by second- and third-order methods; $M = 7.4$, $\alpha = 0°$.

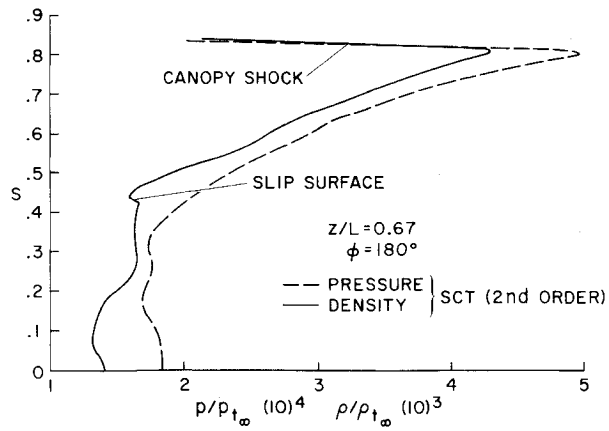

Fig. 7 Radial pressure and density distributions in the leeward plane of symmetry.

compare the noncentered second- and third-order finite-difference schemes for such a calculation, the body shown in Fig. 2 was modeled using 12 longitudinal regions. The flowfield was calculated for Mach 7.4 and 0° angle of attack. These particular flow conditions are of interest computationally because available experimental shadowgraphs[17] show the shock generated by the canopy intersects the nose shock and results in a coalesced shock and slip surface downstream of the intersection. These conditions might also simulate a postlaunch configuration. For this calculation the nose of the vehicle was simulated by a 23.07° pointed cone. The grid size consisted of 29 radial mesh points and 19 meridional mesh points. The calculation, which consisted of 900 streamwise integration steps and covered over 70% of the body, took approximately 48 min for the third-order scheme and 38 min for the second-order scheme on an IBM 360/67. The third-order method proved to take 20% more time for equal grid sizes.

The shock locations in both the planform and side view for the two calculations are compared in Fig. 5 with the experimental shadowgraphs made by Cleary.[17] Both the canopy and main nose shock are predicted quite accurately by both schemes, even though the nose was approximated by a pointed cone. The slip surface or inviscid shear layer, which results when two shocks of the same family intersect, compares favorably with that of the experiment. The shock generated off the leading edge of the wing is in some disagreement with the shadowgraph. This is due to the fact that the actual wing is crudely approximated by a thicker wing in the numerical calculation. In this calculation the integration procedure terminated after calculating over 70% of the flowfield because of numerical difficulties encountered at the body in the region near the wing's leading edge. The flow variables in this vicinity are changing rapidly because of the expanding wing and thus there exist large gradients of these variables. The equally spaced distribution of points in the meridional direction was not sufficient to handle these large gradients and resulted in an unstable solution. Although termination occurred just before the bow shock intersected the wing shock, the calculations in the vicinity of the intersection were behaving normally and were not to blame for the termination. Recent calculations indicate that when a clustering of points is established near the wing leading edge, the method is capable of integrating through the wing shock-bow shock intersection region.

One of the main advantages of the third-order SCT with variable free parameters is its ability to capture weak shocks in the presence of strong shocks with both shocks being well defined. Figure 6 shows the propagation of the canopy shock through the shock layer in the leeward plane of symmetry. Both shock waves in this figure are spread over only two or three mesh intervals and the associated oscillations are minimal. The canopy shock, when it first forms, is at least four times as strong as the bow shock in the same plane. However, the rapid expansion over the aft portion of the canopy quickly weakens its intensity.

Radial pressure and density distributions in the leeward plane behind the canopy shock-bow shock intersection point are shown in Fig. 7. The slip surface appears as a rapid but small change in the density while the corresponding pressure variation in that vicinity remains smooth.

Figure 8 shows a sequence of various longitudinal cross sections through the shock layer. The canopy shock, which formed as a result of a rapid increase in the semiminor axis (b_t) of the top ellipse, is seen to propagate through the shock layer, intersect the bow shock, and then propagate as a coalesced shock beyond the intersection point. The slip surface stretches

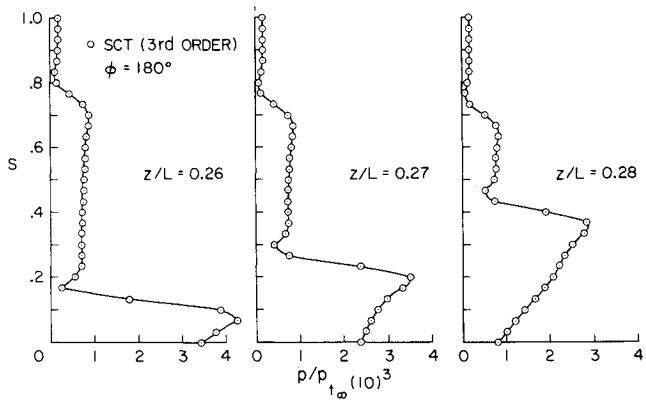

Fig. 6 Propagation of canopy shock through shock layer in the leeward plane; $M = 7.4$, $\alpha = 0°$.

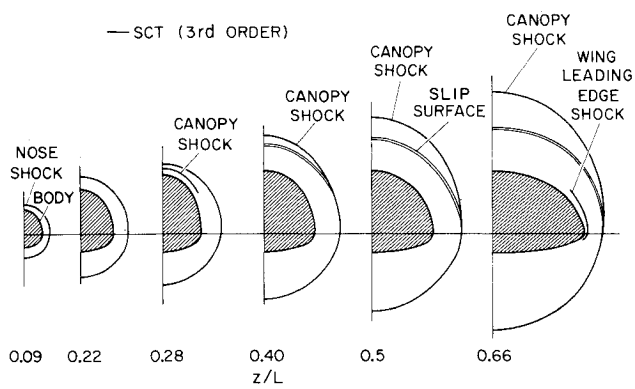

Fig. 8 Cross-sectional shock shapes at various longitudinal stations of shuttlelike configurations; $M = 7.4$, $\alpha = 0°$.

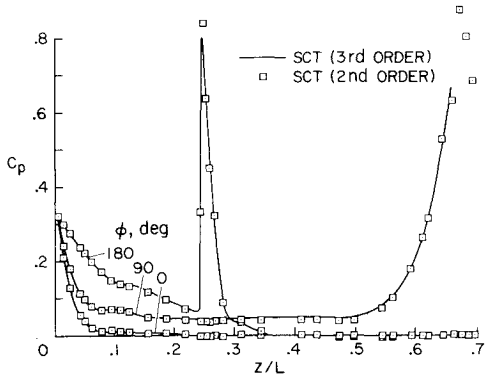

Fig. 9 Longitudinal surface pressure distributions for the 0°, 90°, and 180° meridians of shuttlelike configuration; $M = 7.4$, $\alpha = 0°$.

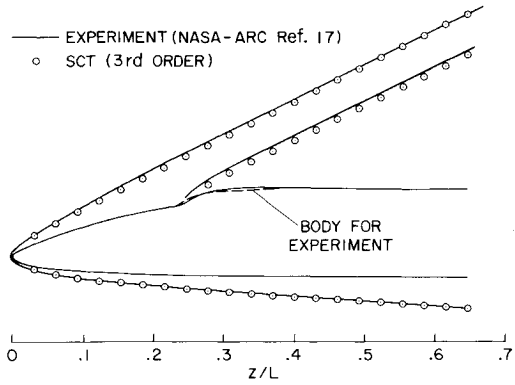

Fig. 11 Shock location for a blunted shuttlelike configuration; $M = 7.4$, $\alpha = 15.3°$.

from the shock-shock intersection point to the leeward plane of symmetry. The wing leading edge shock, because of the 0° angle-of-attack condition, appears mainly on the leeward or top part of the body and dissipates quickly as it extends toward the bottom.

A comparison of the surface pressure distribution in the longitudinal direction for the 0°, 90°, and 180° meridians between the second- and third-order schemes is shown in Fig. 9. The deviations between the two methods is slight. The rather substantial pressure rise near z/L of 0.25 is a result of the canopy. This strong compression, however, is quickly followed by an equally strong expansion. The rapid rise in pressure starting at z/L of 0.5 in the 90° meridian is a result of the wing.

Figure 10 shows the streamline distributions on the lower surface of the SSV for the region calculated. The crossflow direction is evident in this figure.

To calculate a blunt-nosed configuration, the inverse blunt-body code of Lomax and Inouye[4] was used as the starting solution. The SCT code employing the third-order algorithm was then used to integrate the equations downstream from this starting plane. The results of such a calculation are shown in Figs. 11 and 12 for a shuttle orbiter in Mach 7.4 flow at 15.3° angle of attack. Figure 11 exhibits the shock shapes in the windward and leeward planes, including the canopy shock, and compares them with the experimental shadowgraphs. The shadowgraph experiment was actually performed at 15° angle of attack, but the surface pressure experiment, which we were more interested in, was run at 15.3°. The location of the nose shock agrees quite well with the experiment; however, there is some disagreement in location of the canopy shock between the numerical and experiment. The main reason for this is that the canopy in the shadowgraph model was slightly displaced from that of the pressure and heat-transfer model from which the numerical body was copied. If this displacement is accounted for, then both shocks line up with each other.

The longitudinal surface pressure distribution for the 0°, 90°, and 180° planes is shown in Fig. 12. A detailed comparison between these numerical results, the method of characteristics, and the experiment can be found in Ref. 18. In that paper results are presented which show that the entropy layer is adequately described.

Concluding Remarks

The results obtained by applying the SCT code to a complicated three-dimensional shuttle-like configuration indicate that it is capable of accurately predicting the inviscid flowfield structure from the nose of the vehicle to a point upstream of the final swept position of the wing. The fixed grid of equally spaced points in the meridional direction is not capable of resolving entirely the flow in the vicinity of the wing leading edge, and this has hampered the calculations over the remaining portion of the body. Recent results have indicated, however, that a concentration of points in that region, by either an independent variable transformation or simply the addition of points, will alleviate the difficulty and allow the integration to proceed further down the body.

The calculations have shown that when the body used in the experiments is properly modeled numerically, the location of all shock waves agrees well with the experimental shadowgraphs. The method was shown to be capable of handling the shock-shock intersection problem, such as occurs when the canopy shock intersects the nose shock, with little or no difficulty.

Both second- and third-order noncentered difference algorithms were used to integrate the governing equations. The coding of these schemes is facilitated by the fact that the dependent variables are only evaluated on the primary mesh, i.e., no staggered mesh is required; in addition, the algorithms themselves are relatively simple in appearance and are readily programed. The final step in the third-order scheme, Eq. (11c), appears rather complicated since the free parameter ω was

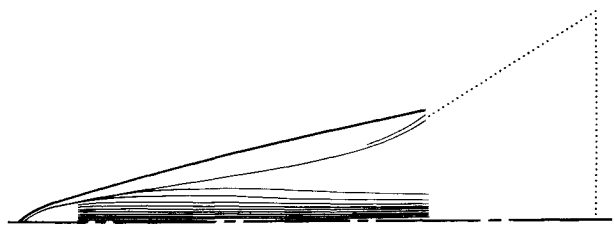

Fig. 10 Surface streamline distribution on bottom of shuttlelike configuration; $M = 7.4$, $\alpha = 0°$.

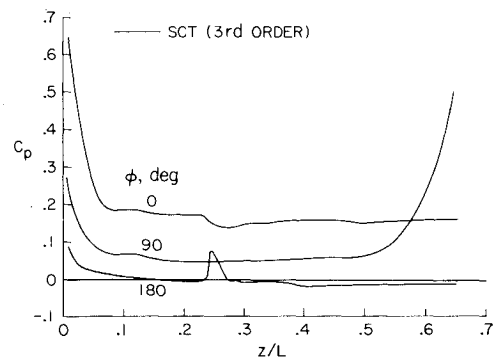

Fig. 12 Longitudinal surface pressure distribution for shuttlelike configuration at $M = 7.4$, $\alpha = 15.3°$.

considered to be spatially dependent. This complication is more apparent than real, and it is believed that local control of dispersive and dissipative errors is worth the slight increase in arithmetic if one desires to utilize a third-order method.

In some of the examples cited it was shown that the third-order scheme is capable of coping with some of the critical regions of the flowfield which apparently caused termination of the second-order scheme. The shock waves that existed or formed using the third-order scheme with variable free parameters were well defined and the post and precursor oscillations were minimal.

References

[1] Kutler, P., "Application of Selected Finite Difference Techniques to the Solution of Conical Flow Problems," Ph.D. thesis, 1969, Iowa State Univ., Dept. of Aerospace Engineering, Ames, Iowa.

[2] Kutler, P. and Lomax, H., "Shock-Capturing, Finite Difference Approach to Supersonic Flows," *Journal of Spacecraft and Rockets*, Vol. 8, No. 12, Dec. 1971, pp. 1175–1187.

[3] Warming, R. F., Kutler, P., and Lomax, H., "Second- and Third-Order Noncentered Difference Schemes for Nonlinear Hyperbolic Equations," *AIAA Journal*, Vol. 11, No. 2, Feb. 1973, pp. 189–196.

[4] Lomax, H. and Inouye, M., "Numerical Analysis of Flow Properties About Blunt Bodies Moving at Supersonic Speeds in an Equilibrium Gas," TR R-204, 1964, NASA.

[5] Rakich, J. V., "Three-Dimensional Flow Calculations by the Method of Characteristics," *AIAA Journal*, Vol. 5, No. 10, Oct. 1967, pp. 1906–1908.

[6] MacCormack, R. W., "The Effect of Viscosity in Hypervelocity Impact Cratering," AIAA Paper 69-354, Cincinatti, Ohio, 1969.

[7] Thomas, P. D., "On the Computation of Boundary Conditions in Finite Difference Solutions for Multi-Dimensional Inviscid Flow Fields," LMSC 6-82-71-3, March 1971, Lockheed Palo Alto Research Lab., Palo Alto, Calif.

[8] Morretti, G., "The Importance of Boundary Conditions in the Numerical Treatment of Hyperbolic Equations," *The Physics of Fluids*, Supplement II, Vol. 12, No. 12, Dec. 1969, pp. II-13–II-20.

[9] Kentzer, C. P., "Discretization of Boundary Conditions on Moving Discontinuities," *Proceedings of the Second International Conference on Numerical Methods in Fluid Dynamics*, edited by M. Holt, Springer-Verlag, Berlin, 1971; pp. 108–113.

[10] Burstein, S. Z., "Numerical Methods in Multidimensional Shocked Flows," *AIAA Journal*, Vol. 2, No. 12, Dec. 1964, pp. 2111–2117.

[11] Abbett, M. J., "Boundary Condition Computational Procedures for Inviscid Supersonic Steady Flow Field Calculations," Final Rept. 71-41, 1971, Aerotherm Corp., Mt. View, Calif.

[12] Ames Research Staff, "Equations, Tables, and Charts for Compressible Flow," Rept. 1135, May 1953, NACA.

[13] Kutler, P. and Lomax, H., "The Computation of Supersonic Flow Fields About Wing-Body Combinations by 'Shock-Capturing' Finite Difference Techniques," *Proceedings of the Second International Conference on Numerical Methods in Fluid Dynamics*, edited by M. Holt, Springer-Verlag, Berlin, 1971, pp. 24–29.

[14] Morretti, G. and Abbett, M., "A Time-Dependent Computational Method for Blunt Body Flows," *AIAA Journal*, Vol. 4, No. 12, Dec. 1966, pp. 2136–2141.

[15] Bohachevsky, I. O. and Mates, R. E., "A Direct Method for Calculation of the Flow About an Axisymmetric Blunt Body at Angle of Attack," *AIAA Journal*, Vol. 4, No. 5, May 1966, pp. 776–782.

[16] Babenko, K. I. et al., "Three-Dimensional Flow of Ideal Gas Past Smooth Bodies," TT F-380, April 1966, NASA.

[17] Cleary, J. W., "Hypersonic Shock-Wave Phenomena of a Delta-Wing Space-Shuttle Orbiter," TM X-62,076, Oct. 1971, NASA.

[18] Rakich, J. V. and Kutler, P., "Comparison of Characteristic and Shock Capturing Methods with Application to the Space Shuttle," AIAA Paper 72-191, San Diego, Calif., 1972.